A tunable Fabry-Pérot quantum Hall interferometer in graphene

Corentin Déprez, Louis Veyrat, Hadrien Vignaud, Goutham Nayak, Kenji Watanabe,
Takashi Taniguchi, Frédéric Gay, Hermann Sellier, and Benjamin Sacépé

I. SAMPLES STUDIED

Figure S1 displays optical images of the devices studied in this work. The fabrication process is described in Methods. The thickness of the van der Waals layers and the size of the split-gate gaps are reported in Table S1.

Sample	Top hBN thickness (nm)	Bottom hBN thickness (nm)	Graphite thickness (nm)	Split-gate gap (nm)
BNGr74	22	18	4	0 / 21 / 20
BNGr64	20	50		148 / 159
BNGr30	25	15		129 / 140

TABLE S1: **Samples characteristics.** The thickness of the hBN and graphite layers are measured by atomic force microscopy. The gap size of the split-gate electrodes is measured by scanning electron microscopy.

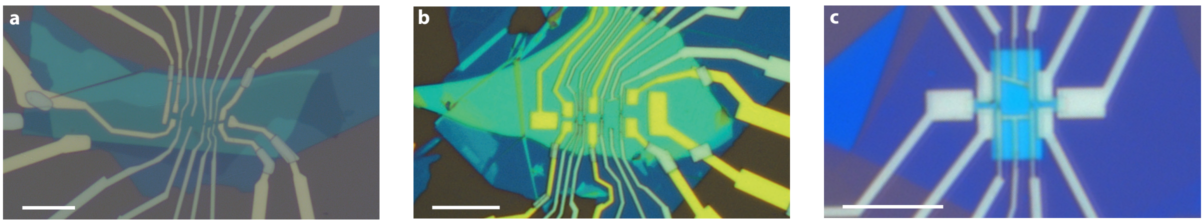

FIG. S1: **Optical images of the devices. a,** Sample BNGr74 of the main text. **b,** Sample BNGr64 described in section XII. **c,** Sample BNGr30 described in section XII. Scale bars are 10 μm.

II. PARAMETERS EXTRACTED FROM THE AHARONOV-BOHM INTERFERENCE

Table S2 presents the various parameters extracted from the measurements shown in Figure 3 of the main text, among which the Aharonov-Bohm period $\Delta B_{@14\,\mathrm{T}}$, the Thouless energy E_{Th} extracted from the checkerboard patterns, the energy scale T_0 related to the temperature dependence of the resistance oscillation, together with the geometrical dimensions (surfaces and lengths between QPCs) of the three Fabry-Pérot cavities.

Importantly, we stress that the determination of the device geometry relies on optical images of the graphene flake taken during the van der Waals pick up process, which makes the exact determination of the graphene edge delicate. We therefore assess the graphene edge position from this image at ± 150 nm, which results in the uncertainties of the geometrical area A_{geo} of the FP cavities and lengths L between QPCs reported in Table S2.

QH-FP	$\Delta B_{@14\,\mathrm{T}}$ (mT)	A_{AB} (μm^2)	A_{geo} (μm^2)	L (μm)	E_{Th} (μV)	T_0 (mK)	$E_{\mathrm{Th}}/4\pi^2 k_{\mathrm{B}}$ (mK)
Small	1.32	3.1	3.1 ± 0.4	4.3 ± 0.5	134	43	39
Medium	0.40	10.4	10.7 ± 1.2	7.2 ± 0.5	83	20	24
Large	0.27	15.0	13.1 ± 1.8	9.0 ± 0.5	57	14	17

TABLE S2: **Geometrical and physical parameters corresponding to the measurements of Fig. 3.** Aharonov-Bohm period $\Delta B_{@14\,\mathrm{T}}$ obtained at $B = 14$ T and resulting Aharonov-Bohm area A_{AB}; geometrical area A_{geo} of the FP cavities; geometrical length L between two QPCs of the cavity; Thouless energy E_{Th} extracted from the checkerboard patterns in Fig. 3c and d; Energy scale T_0 extracted from Fig. 3h; $E_{\mathrm{Th}}/4\pi^2 k_{\mathrm{B}}$, the quantity theoretically equal to T_0 according to ref.[1]

III. DESIGN CHARACTERISTIC OF THE QPCS

The presence of the graphite back-gate electrode separated from the graphene by a thin hBN dielectric layer imposes drastic conditions for the design of the split-gate electrodes. Contrary to devices on Si/SiO_2 studied in ref.[2,3] in which the split-gate gap of about 150 nm led to a suitable ratio of split-gate capacitance to QPC capacitance, the very close proximity of the graphite back gate imposes a much smaller split-gate gap. By performing numerical simulations[3], we estimated the split-gate gap that leads to a ratio of split-gate capacitance to QPC capacitance of the order of 2 to be of the order of few tens of nanometers, depending on the hBN thicknesses. Figure S2 displays scanning electron micrographs of the three split gates of sample BNGr74 discussed in the main text. The split-gate gaps of QPC_2 and QPC_3 are 20 nm, suitable for operating the split gates as QPCs in the quantum Hall regime. The split-gate electrodes of QPC_1 are unintentionally connected but this short-circuit does not hinder QPC operation (see QPC characterizations in section VI).

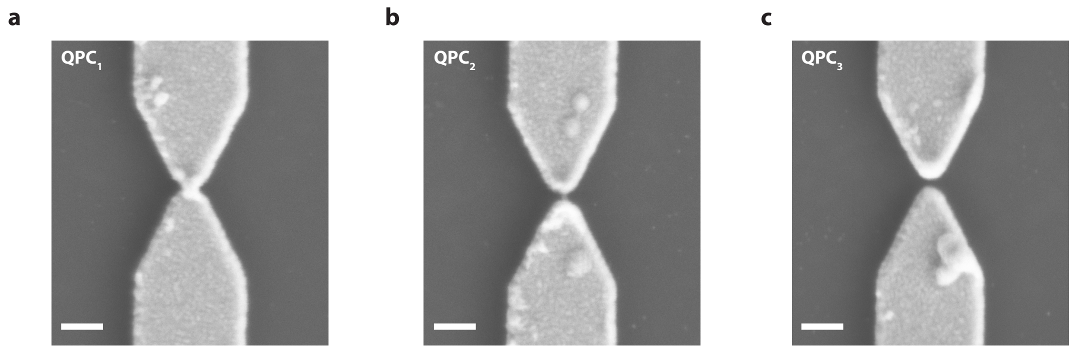

FIG. S2: **QPCs geometry.** Scanning electron micrograph of the QPCs of BNGr74 device. **a,** QPC_1. **b,** QPC_2. **c,** QPC_3. The two split-gate electrodes of QPC_1 are unintentionally connected. The gaps between the two other split gates is 20 nm. Scale bar is 100 nm.

IV. CHARACTERIZATION OF THE SPLIT-GATE CAPACITANCES AT 0 T

In this section, we present the characterization of the back gate and the different split gates at zero magnetic field for the sample of the main text. Figure S3 shows color-coded maps of the longitudinal resistance $R_{\rm xx}$ versus back-gate voltage $V_{\rm bg}$ and voltage $V_{\rm QPC}$ applied on a split gate (other split gates are floating). The maps exhibit four quadrants separated by two nearby horizontal lines and a diagonal line. The most resistive horizontal line, at $V_{\rm bg} = -0.04$ V, corresponds to the charge neutrality point in the bulk of graphene and the diagonal line corresponds to the charge neutrality point below the active split-gate electrodes, as usual for graphene devices equipped with a local top gate. The two lines intersect at $V_{\rm QPC} \simeq +0.38$ V as a result of the work function difference between the palladium of the gates and the graphene. The second horizontal line is more unusual and results from the local hole doping of the graphene beneath the two other split gates that are not active but contribute in series to the measured resistance. The palladium of these split-gate electrodes shifts the position of the charge neutrality point beneath them to $V_{\rm bg} = 0.12-0.18$ V, yielding a secondary resistance peak, independent of the active split gate and observed consistently for the three QPC maps. These maps also provide the capacitance ratios $C_{\rm sg}/C_{\rm bg}$ between the active split-gate and the back-gate electrodes which are respectively 0.83 for $\rm QPC_1$ and 0.86 for $\rm QPC_2$ and $\rm QPC_3$. They are important quantities for the analysis of the QPC properties in the QH regime.

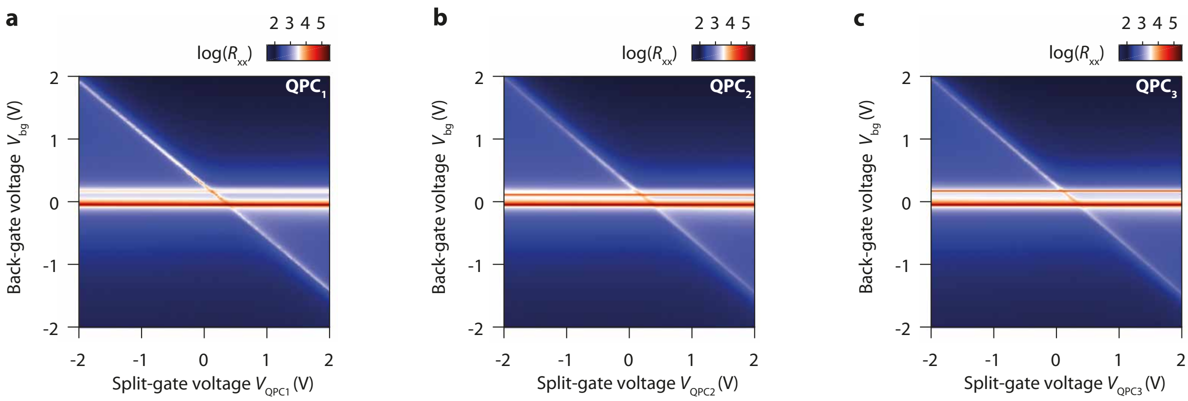

FIG. S3: **Split-gates characterization at 0 T. a, b, c,** Longitudinal resistance $R_{\rm xx}$ versus split-gate voltage $V_{\rm QPC}$ and back-gate voltage $V_{\rm bg}$ for the three QPCs of the QH-FP interferometer presented in the main text. The horizontal line at $V_{\rm bg} = -0.04$ V corresponds to the charge neutrality point in the bulk graphene, whereas the diagonal lines correspond to the charge neutrality point in the graphene beneath the active split gate. These lines intersect at $(V_{\rm QPC}, V_{\rm bg}) \simeq (+0.38\ {\rm V}, -0.04\ {\rm V})$ revealing the significant local hole doping induced by the palladium gates. The second horizontal line at $V_{\rm bg} = 0.18$ V in a and c and $V_{\rm bg} = 0.12$ V in b marks the positive back-gate voltage needed to compensate the hole doping induced by the palladium beneath the non-active split gates.

V. FAN DIAGRAM OF BULK LANDAU LEVELS

In this section, we present the Landau fan diagram of sample BNGr74. Fig. S4 displays the longitudinal resistance R_{xx} as a function of magnetic field B and back-gate voltage V_{bg}, measured at 0.02 K. This measurement was performed with a voltage $V_{\mathrm{QPC}} = +0.3$ V applied on each QPC to compensate the hole doping induced by the palladium split gates and ensure a quasi-homogeneous charge carrier density in the graphene layer.

Broken-symmetry states in electron(hole)-type Landau levels emerge as minima in R_{xx} above 5 T (3 T), consistent with the mobility $\mu = 130\,000\,\mathrm{cm}^2.\mathrm{V}^{-1}.\mathrm{s}^{-1}$ obtained for a charge carrier density of $1 \times 10^{12}\,\mathrm{cm}^{-2}$ from Hall measurements. In addition, an insulating behaviour develops at charge neutrality with increasing magnetic field. The full-lifting of the degeneracies in the zeroth Landau level occurs above 4 T, allowing to perform interferometry experiments with the inner or outer electron edge channels of the zeroth Landau level at relatively low magnetic field values (see section XI).

From the position of the R_{xx} minima, we extract a back-gate capacitance $C_{\mathrm{bg}} = 1.45\,\mathrm{mF/m}^2$ consistent with the bottom hBN thickness and a hBN dielectric constant $\epsilon_{\mathrm{r}}^{\mathrm{BN}} \approx 3$.

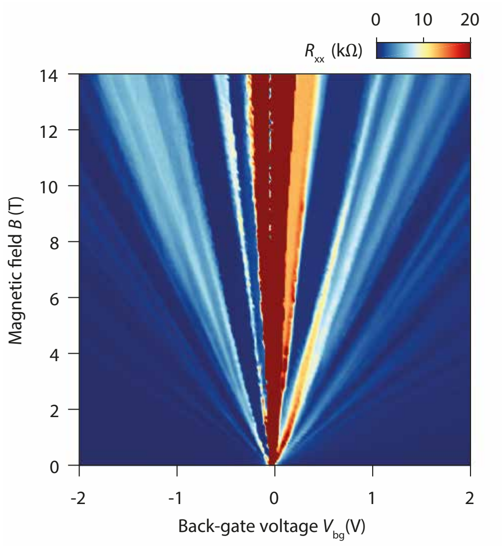

FIG. S4: **Landau fan diagram.** Longitudinal resistance R_{xx} of sample BNGr74 (device of the main text) versus back-gate voltage V_{bg} and magnetic field B, measured at 0.02 K.

VI. CHARACTERIZATION OF THE QPCS IN THE QUANTUM HALL REGIME

QH interferometry experiments require a precise knowledge of the edge-channels configuration in the bulk of graphene, beneath the split-gate electrodes and in the split-gate constrictions. This section describes the action of the split-gate electrodes in the QH regime, which allows to determine the gate-voltage set points for the (partial) QPC pinch-off and tuning of QH edge channel transmissions.

Extended Data Figure 1 displays the diagonal conductance G_D as a function of split-gate and back-gate voltages, V_QPC and V_bg, for the three QPCs. The three conductance maps show features similar to those reported in ref.[2] for a QPC operating in the QH regime. At negative split-gate voltages, G_D draws diagonal strips of nearly constant and quantized values. They have a smaller slope than the zero-field diagonal lines of Fig. S3, indicative of the smaller couplings at the constrictions characterized by capacitance ratios $C_\mathrm{QPC}/C_\mathrm{bg} \simeq 0.58$, 0.31 and 0.36 for QPC_1, QPC_2 and QPC_3, respectively. As demonstrated in ref.[2], the quantized G_D values indicate the number of transmitted QH edge channels through the QPC. For a given bulk filling factor, the QH edge channels can be backscattered by applying a negative split-gate voltage V_QPC. For instance, at $V_\mathrm{bg} = 0.75$ V, the bulk filling factor is $\nu \simeq 2$, leading to the blue rhombi of $G_\mathrm{D} = 2e^2/h$ located near $V_\mathrm{QPC} = 0$ V in Extended Data Fig. 1. Decreasing V_QPC to negative values, the conductance drops to the dark blue strip of $G_\mathrm{D} = e^2/h$, and then to $G_\mathrm{D} = 0$ at even more negative values. These conductance changes reflect the successive backscattering of the QH edge channels at the QPC[2]. The linecuts of Extended Data Fig. 2 further illustrate such a successive pinch off of the inner and outer edge channels at $\nu \simeq 2.5$ (Extended Data Fig. 2a) and the pinch off the outer edge channel at $\nu \simeq 1.5$ (Extended Data Fig. 2b).

As discussed in section IV, the hole-doped graphene regions beneath the non active split-gate electrodes intervene in the transmission of the whole device when studying the properties of a particular split gate. These hole-doped regions have a lower filling factor than the bulk and can therefore backscatter some bulk QH edge channels. As a consequence, the QH plateaus as a function of back-gate voltage at $V_\mathrm{QPC} \sim 0$ V in the QPC maps of Extended Data Fig. 1 are not centered at the integer bulk filling factors indicated on the right axis and determined by the fan diagram $R_\mathrm{xx}(V_\mathrm{bg}, B)$ at compensated split-gate voltages (see Fig. S4).

The comparison in Fig. S5 between a QPC map and the transverse Hall resistance R_xy that relates to the bulk filling factor bears out this observation. The $\nu = 2$ plateau develops at lower back-gate voltage in the Hall resistance than in the diagonal resistance across the QPCs. Despite the fact that the bulk has two QH edge channels when $1/R_\mathrm{xy} = \frac{2e^2}{h}$ at, for instance, $V_\mathrm{bg} = 0.5$ V, the non active QPCs that have lower filling factors backscatter the inner edge channel leading to $G_\mathrm{D} = e^2/h$ in the QPC conductance map.

Furthermore, for the data presented in the main text, we assessed the number of bulk QH edge channels through the value of the Hall resistance plateau. For all figures of the main text, we measured $1/R_{\mathrm{xy}} = \frac{2e^2}{h}$, which indicates that two edge channels propagate in the graphene bulk.

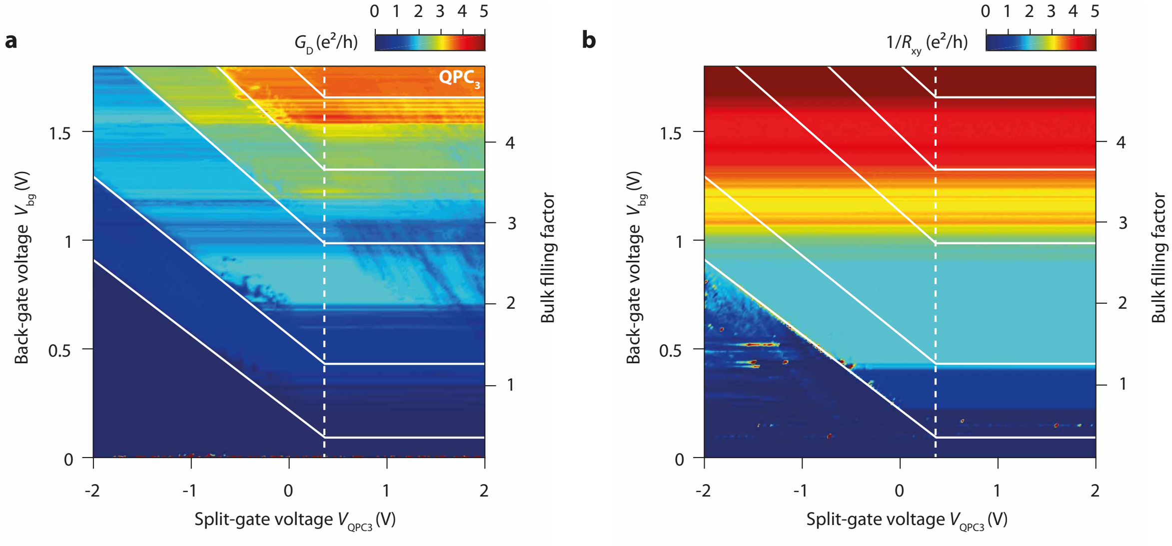

FIG. S5: **QPC map compared to Hall resistance map at 14 T. a,** Diagonal conductance G_{D} versus split-gate voltage, V_{QPC}, and back-gate voltage, V_{bg}, for QPC$_3$. **b,** Inverse of the transverse Hall resistance $1/R_{\mathrm{xy}}$ versus V_{QPC} and V_{bg}. The vertical dashed white line indicates the split-gate voltage that compensates the hole doping induced by the split-gate electrodes (iso-density in the bulk and beneath the active split gate). This voltage is determined in the zero-field maps of Fig. S3 at the intersection between the diagonal line and the main horizontal line of the bulk charge neutrality point. The horizontal solid white lines delineate the quantized plateaus in the Hall resistance that are centered at integer bulk filling factors (indicated on the right axis). The diagonal lines delineate the diagonal strips of constant G_{D} in the QPC map, that is, conductance plateaus given by the number of transmitted edge channels through the QPC (see ref.[2] for a detailed analysis). For consistency, these diagonal lines meet the horizontal ones of the bulk Hall resistance right at their intersect with the vertical line.

VII. AHARONOV-BOHM OSCILLATIONS FOR DIFFERENT CONFIGURATIONS OF MAGNETIC FIELD AND EDGE CHANNELS

In this section we present plots of the Fourier amplitude of the resistance oscillations with $V_{\rm pg2}$ for experiments performed with different interfering edge channels and magnetic fields. In every cases, the frequency of the oscillations $f_{\rm pg2}$ is well defined and shows a clear and continuous decrease while lowering $V_{\rm pg2}$. As expected for the Aharonov-Bohm regime, the frequency of the oscillations increases with the magnetic field at fixed plunger-gate voltage whereas it does not change with the interfering edge channel. A significant component oscillating at twice the Aharonov-Bohm frequency is visible on Fig. S6a. In this case, only the lowest frequency component was used to plot Fig. 2e in the main text.

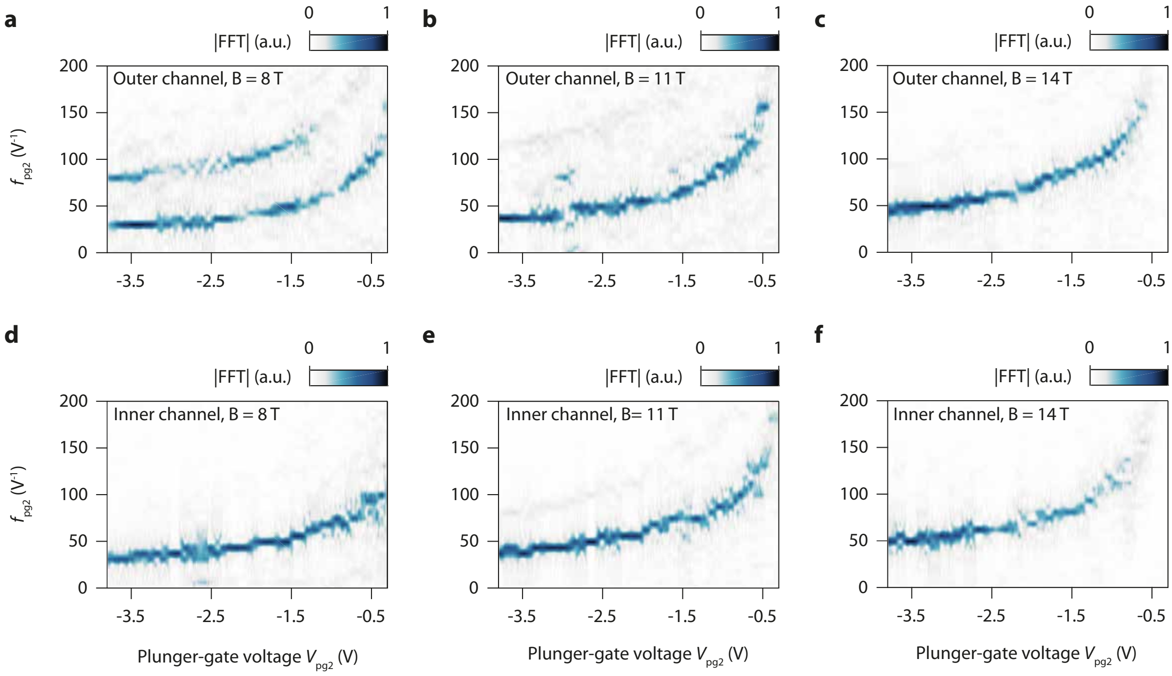

FIG. S6: **Fourier amplitude of the resistance oscillations.** Fourier amplitude of the resistance oscillations observed in the small interferometer for different configurations of magnetic field and interfering edge channel, as a function of plunger-gate voltage $V_{\rm pg2}$ and frequency $f_{\rm pg2}$.

VIII. ELECTROSTATICS OF THE PLUNGER GATE

The potential profile in the graphene below the plunger gate is determined by self-consistent electrostatic simulations in the vertical 2D plane shown in Fig. S7a assuming translational invariance in the third direction. The simulation is done for the same hBN thicknesses as in the device of the main text, with $d_{\mathrm{bottom}} = 18$ nm for the bottom layer and $d_{\mathrm{top}} = 22$ nm for the top layer. The hBN dielectric permittivity $\epsilon_{\mathrm{r}}^{\mathrm{BN}} \approx 3$ is extracted from the position of quantum Hall plateaus versus back-gate voltage. The graphite back-gate is treated as a perfect metal. The graphene sheet is modelled by a charge density $\sigma(x)$ linked to the electrostatic potential $V(x)$ by the relation:

$$\sigma(x) = (-e)\,\mathrm{sign}(V(x))\,\frac{e^2V(x)^2}{\pi\hbar^2 v_{\mathrm{F}}^2}$$

where $v_{\mathrm{F}} = 10^6$ m/s is the Fermi velocity in graphene. The electrostatic problem is solved self-consistently using a modified version of MaxFEM (http://www.usc.es/en/proxectos/maxfem), an electromagnetic simulation software based on the finite-element method. The mesh grid computed using Gmsh (http://gmsh.info) extends 1 μm in vertical and 2 μm in horizontal.

The self-consistent solution $V(x)$ can be calculated for a given back-gate voltage V_{bg} and a series of plunger-gate voltages V_{pg} in order to determine the dependence of the pn interface position x_{pn} on the plunger-gate voltage. Equivalently, the local plunger-gate capacitance $C_{\mathrm{pg}}(x)$ can be extracted from a single self-consistent simulation (for example at $V_{\mathrm{bg}} = 0$ and $V_{\mathrm{pg}} = -1$ V) using the quantum capacitance model[4]. This model is based on the relation between $\sigma(x)$ and $V(x)$ given above, together with the definition of the capacitive couplings:

$$\sigma(x) = -C_{\mathrm{bg}}\left(V_{\mathrm{bg}} - V(x)\right) - C_{\mathrm{pg}}(x)\left(V_{\mathrm{pg}} - V(x)\right)$$

where $C_{\mathrm{bg}} = \epsilon_0\epsilon_{\mathrm{r}}^{\mathrm{BN}}/d_{\mathrm{bottom}}$. This approach based on the determination of the local capacitance $C_{\mathrm{pg}}(x)$ has the advantage to provide the self-consistent solution for any set of back-gate and plunger-gate voltages without the need to solve again the full electrostatic problem.

The spatial variation of the potential energy $E(x) = -eV(x)$ below the plunger gate is plotted in Fig. S7b for a fixed back-gate voltage $V_{\mathrm{bg}} = 0.53$ V and various negative plunger-gate voltages corresponding to the experiment reported in Fig. 2 of the main text. The position x_{pn} of the pn interface with respect to the gate edge is plotted in Fig. S7c as a function of the plunger-gate voltage, showing the following behavior: the formation of the pn interface occurs at $V_{\mathrm{pg}} = -0.65$ V (in the data this happens around $\simeq -0.3$ V instead, due to the hole doping of $+0.38$ V from the palladium split-gate electrodes, corresponding to the charge neutrality point below the plunger gate), then the fast displacement of the pn interface corresponds to

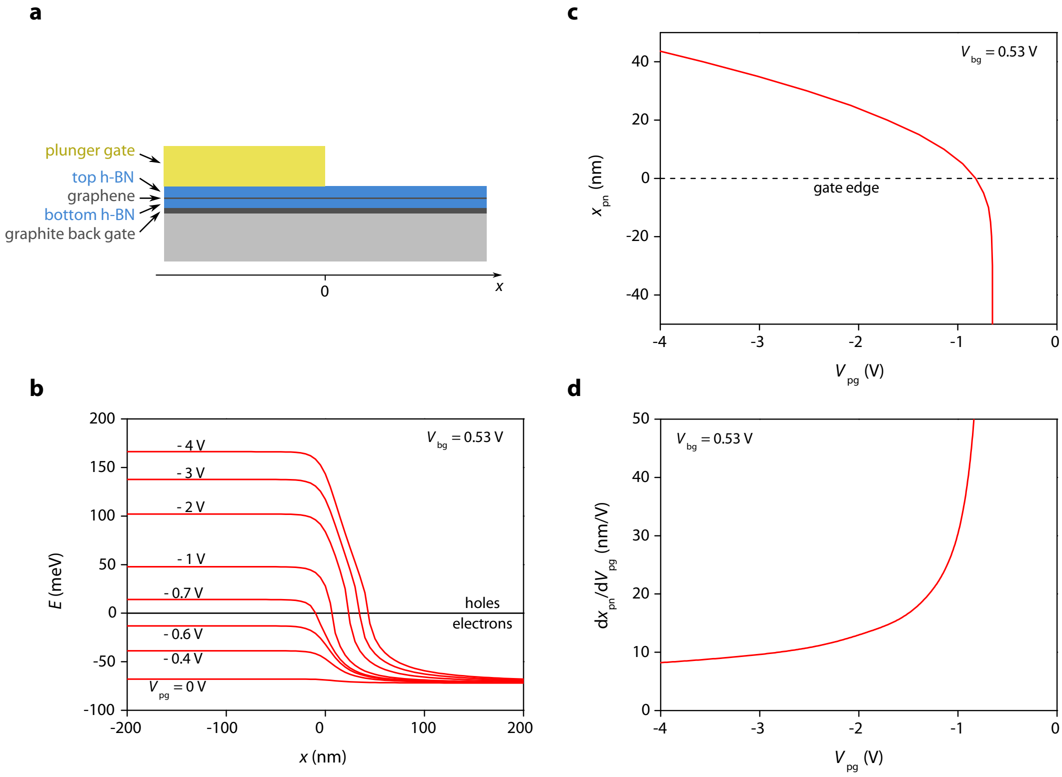

FIG. S7: **Plunger-gate electrostatics. a,** Schematics of the hBN/graphene/hBN heterostructure deposited on the graphite back gate and partially covered by the metallic plunger gate used to tune the interfering path length. **b,** Self-consistent electrostatic energy profiles $E = -eV$ in the graphene layer for a back-gate voltage $V_{\mathrm{bg}} = 0.53$ V and plunger-gate voltages V_{pg} varying from 0 to -4 V. **c,** Position of the pn interface with respect to the gate edge as a function of the plunger-gate voltage. **d,** Displacement rate of the pn interface calculated as its derivative with respect to the plunger-gate voltage.

the expulsion of the pn interface from below the plunger gate, and finally the pn interface moves slower and slower for large negative plunger-gate voltages. The displacement rate $\frac{\mathrm{d}x_{\mathrm{pn}}}{\mathrm{d}V_{\mathrm{pg}}}$ plotted in Fig. S7d is used in the main text to calculate the non-linear lever arm $\alpha = L_{\mathrm{pg}} \times \frac{\mathrm{d}x_{\mathrm{pn}}}{\mathrm{d}V_{\mathrm{pg}}}$ of the plunger gate with contour length L_{pg}. This lever arm provides the theoretical conversion between plunger-gate voltage and interferometer area, which writes $\Delta A = \alpha\,\Delta V_{\mathrm{pg}}$, and which is compared in Fig. 2f with the oscillation frequency measured experimentally. L_{pg} remains an adjustable parameter because the position of the graphene edges is known with an uncertainty of ± 150 nm. To reproduce the measurement, a plunger-gate contour $L_{\mathrm{pg}} = 1.8$ μm is used, in good agreement with the expected lithographic length of 1.5 ± 0.3 μm (the uncertainty of the graphene edge position contributes twice).

IX. AHARONOV-BOHM OSCILLATIONS IN THE MEDIUM INTERFEROMETER

To complement the $(\delta B, V_{\rm pg})$ maps shown in Fig. 3a and b for the small and large interferometers, we present in Fig. S8 the map obtained for the medium interferometer, in the same conditions, i.e. with the outer edge state at $B = 14$ T. The constant resistance lines have a negative slope indicating the Aharonov-Bohm origin of the oscillations. The field periodicity is 0.40 mT corresponding to an Aharonov-Bohm area of 10.4 $\mu\mathrm{m}^2$ in good agreement with the expected lithographic area (see Table S2).

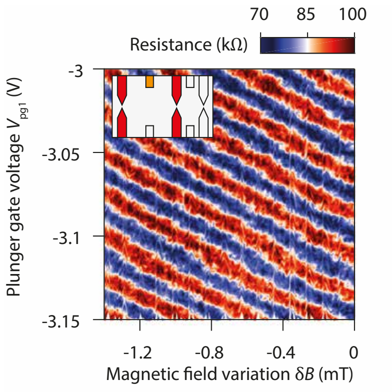

FIG. S8: **Aharonov-Bohm oscillations in the medium interferometer.** Diagonal resistance as a function of plunger-gate voltage $V_{\rm pg2}$ and magnetic field variation δB in the medium interferometer measured at 14 T with the outer edge channel interfering. The inset schematic indicates the active QPCs (in red) and plunger gate (in orange).

X. INTERFEROMETRY EXPERIMENTS WITH INNER EDGE STATE AT 14 T IN THE THREE INTERFEROMETERS

In this section we present additional interferometry experiments performed with the inner edge channel of the zeroth Landau level at $B = 14$ T. Fig. S9a, b and c show the diagonal resistance of the device as a function of plunger-gate voltages and magnetic field for the small, medium and large interferometers, respectively. The results are virtually identical to those performed with the outer edge channel. The magnetic field periods extracted from these measurements are respectively of 1.23, 0.39 and 0.27 mT.

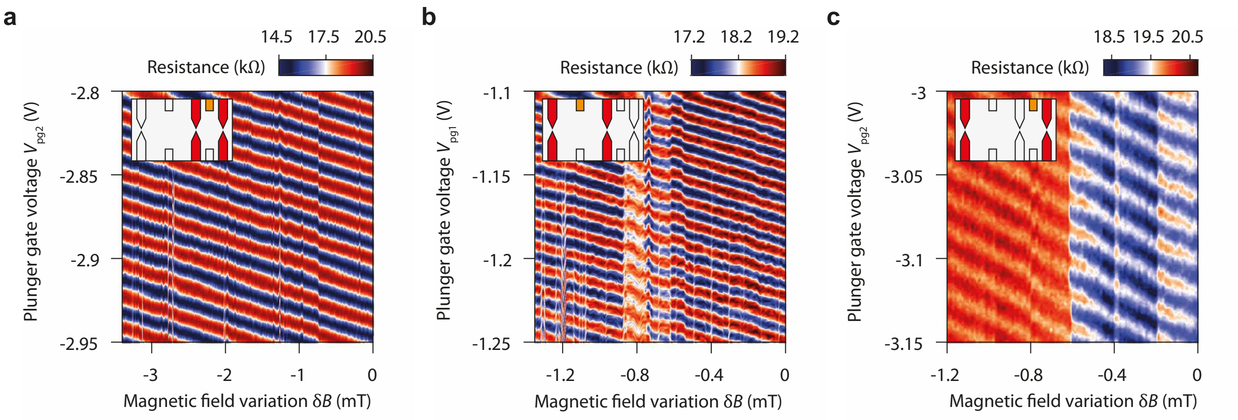

FIG. S9: **Aharonov-Bohm oscillations with the inner edge channel. a, b, c,** Diagonal resistance versus plunger-gate voltage $V_{\mathrm{pg}1,2}$ and magnetic field δB for the small, medium and large interferometers, respectively, with the inner edge channel interfering at 14 T. The inset schematics indicate the active QPCs (in red) and plunger gates (in orange).

XI. INTERFERENCES AT LOWER MAGNETIC FIELDS

Here we show that the device BNGr74 presented in the main text can also operate at low magnetic field. Stable Aharonov-Bohm interference were observed with the outer and inner edge channels respectively down to 5 T and 4 T as displayed in Fig. S10a and b. The respective Fourier amplitudes of the resistance oscillations are shown in Fig. S10c and d.

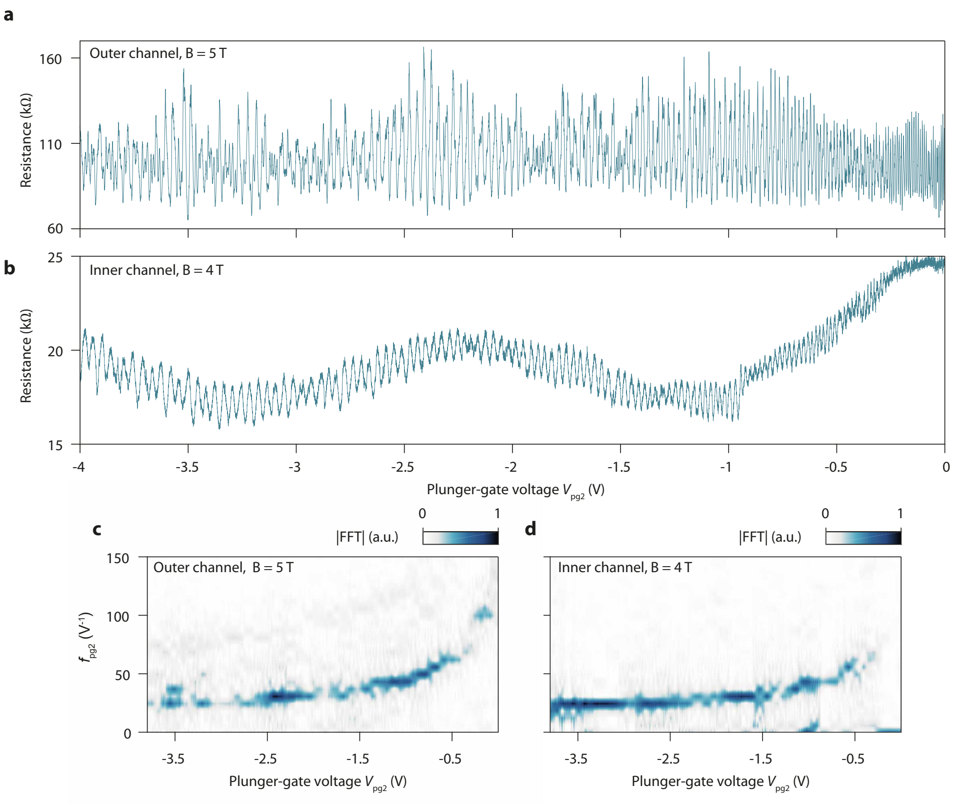

FIG. S10: **Resistance oscillations at low magnetic fields. a, b,** Resistance oscillations as a function of plunger-gate voltage V_{pg2} measured in the small interferometer at 5 T with the outer edge channel, and 4 T with the inner edge channel, respectively. **c, d,** Fourier amplitude of the resistance oscillations in a and b.

XII. AHARONOV-BOHM OSCILLATIONS IN OTHER DEVICES

In this section we present the data obtained on two other devices, BNGr64 and BNGr30. They do not have a graphite back gate, and the silicon substrate serves as the back gate instead. Even without graphite electrode, we observed for both samples Aharonov-Bohm oscillations, indicating that the absence of charging effect is not only related to the screening by the graphite gate.

BNGr64 device

We first present the data for the device BNGr64 shown in Fig. S1b. In this device, three out of four QPCs were operating correctly enabling us to perform experiments with only one of the two interferometers, whose scanning electron micrograph is displayed in Fig. S11. This device was studied using a larger ac bias-voltage excitation of 20 μV and using the bottom plunger gate. The large plunger gate was kept grounded during the measurements.

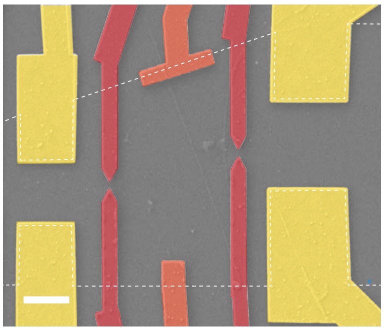

FIG. S11: **QH-FP interferometer in sample BNGr64.** False-colored scanning electron micrograph of the device. Graphene edges are represented by the white dotted line. Contacts, QPCs and plunger gates are color-coded in yellow, red and orange. Scale bar is 1 μm.

We present interferometry experiments performed with the outer interfering edge channel at 14 T with a bulk filling factor $\nu_b = 1.1$. Contrary to the data presented in the main text, there is only one electron-like edge channel propagating in the interferometer. Fig. S12c shows the evolution of the diagonal resistance with plunger-gate voltage $V_{\rm pg}$. Clear resistance oscillations are observed while decreasing $V_{\rm pg}$ from 0 to -3.2 V. Contrary to the data presented in Fig. 2c of the main text, the oscillations show many phase shifts as well as some visibility losses, reflecting the lower degree of stability and coherence of the device. The visibility of the oscillations is typically about 15% as evidenced in Fig. S12a and b. The Fourier transform amplitude of the oscillations is presented in Fig. S12d and shows a decrease of the frequency of the oscillations $f_{\rm pg}$ with the plunger-gate voltage $V_{\rm pg}$ consistent with that in Fig. 2 of the main text.

The evolution of the diagonal resistance oscillations with both the plunger-gate voltage and the magnetic field in this configuration is shown in Fig. S12e. A smooth resistance background for each sweep was subtracted to evidence lines of constant Aharonov-Bohm phase and get rid of average-conductance variations. Constant resistance values form lines with a negative slope in the δB–V_{pg} plane which shows that this device operates in the Aharonov-Bohm regime. From these measurements, we extract a magnetic field period of 0.42 mT corresponding to an enclosed area of 9.9 μm^2 in agreement with the geometrical surface of 11.5 μm^2.

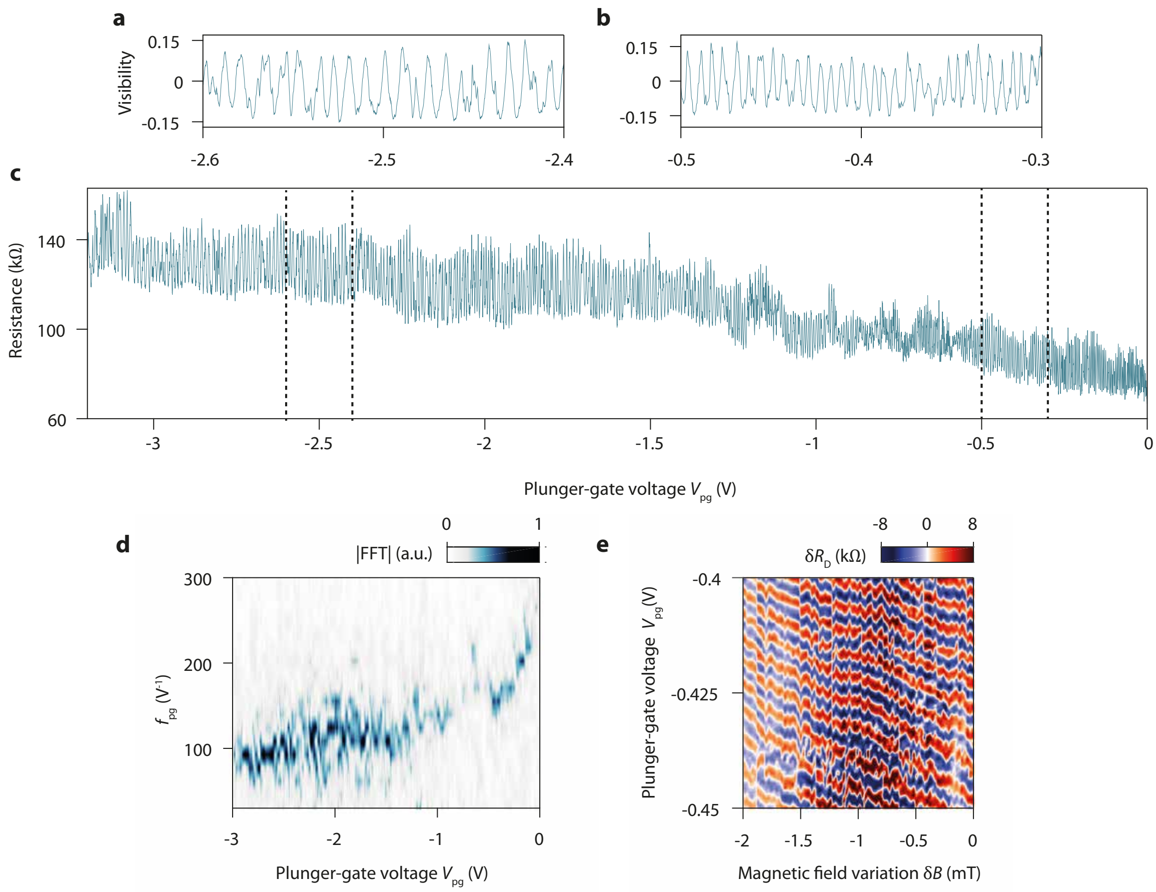

FIG. S12: **Resistance oscillations in sample BNGr64. a, b, c,** Resistance oscillations induced by change of the plunger-gate voltage V_{pg} in interferometry experiments with the inner edge channel at 14 T. Clear resistance oscillations are visible lowering V_{pg}, on top of a continuous increase of the mean resistance of the device evidenced in c. a and b show zooms on smaller V_{pg2} ranges of the resistance oscillations converted in visibility $(R - \bar{R})/\bar{R}$, where $\bar{R}$ is the resistance background. **d,** Amplitude of the Fourier transform of resistance oscillations presented in c with respect to the plunger-gate voltage V_{pg} and the frequency f_{pg}. A continuous decrease of the oscillations frequency is observed while decreasing V_{pg}. **e,** Evolution of the resistance oscillations as function of the plunger-gate voltage V_{pg} and the magnetic field variation δB after subtraction of a resistance background for each plunger-gate voltage sweep. Constant δR_{D} lines have a negative slope characteristic of oscillations induced by Aharonov-Bohm effect.

BNGr30 device

Here we present the data for the device BNGr30, displayed in Fig. S1c. Contrary to the two previous samples, before the deposition of the metallic contacts and of the gates, the heterostructure was etched and shaped using a hard-mask of HSQ resist to uncover the graphene edges at determined positions. After a second e-beam lithography steps, both the contacts and the split gates were made by depositing a Cr/Au bilayer. In this device, the plunger gates cover nearly all the graphene edges between the two QPCs. A scanning electron micrograph of the device is shown in Fig. S13.

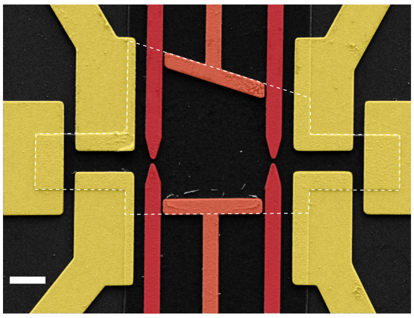

FIG. S13: **QH-FP interferometer in sample BNGr30.** False-colored scanning electron micrograph of the device. Graphene edges are represented by the white dotted line. Contacts, QPCs and plunger gates are color-coded in yellow, red and orange, respectively. Scale bar is 1 μm.

Interferometry experiments performed in this device with the inner edge channel at bulk filling factor $\nu_b = 2.3$ and 14 T are presented in Fig. S14. Resistance oscillations induced by a change of the top plunger-gate voltage V_{pg} are shown in Fig. S14a-c. They appear on the entire range of V_{pg} voltage even though the stability of the QPC is affected by the value of V_{pg}. These oscillations have a small visibility typically varying between 2 and 5 % as shown in Fig. S14a and b. The Fourier transform analysis of the oscillations, shown in Fig. S14d reveals a similar lowering of the frequency f_{pg} of the oscillations with the plunger-gate voltage (the absence of well-defined frequency for the oscillations at $V_{\mathrm{pg}} \simeq -1.2$ V arises from the rapid drop of the resistance background).

In Fig. S14e, we show the evolution of resistance oscillations with both the magnetic field and the plunger-gate voltage. The constant phase lines have a negative slope evidencing that the oscillations result from the Aharonov-Bohm effect. We can extract a magnetic field period of 0.37 mT corresponding to an area enclosed by the interfering edge state of 11.2 $\mu\mathrm{m}^2$ in good agreement with geometric area of 10.1 $\mu\mathrm{m}^2$.

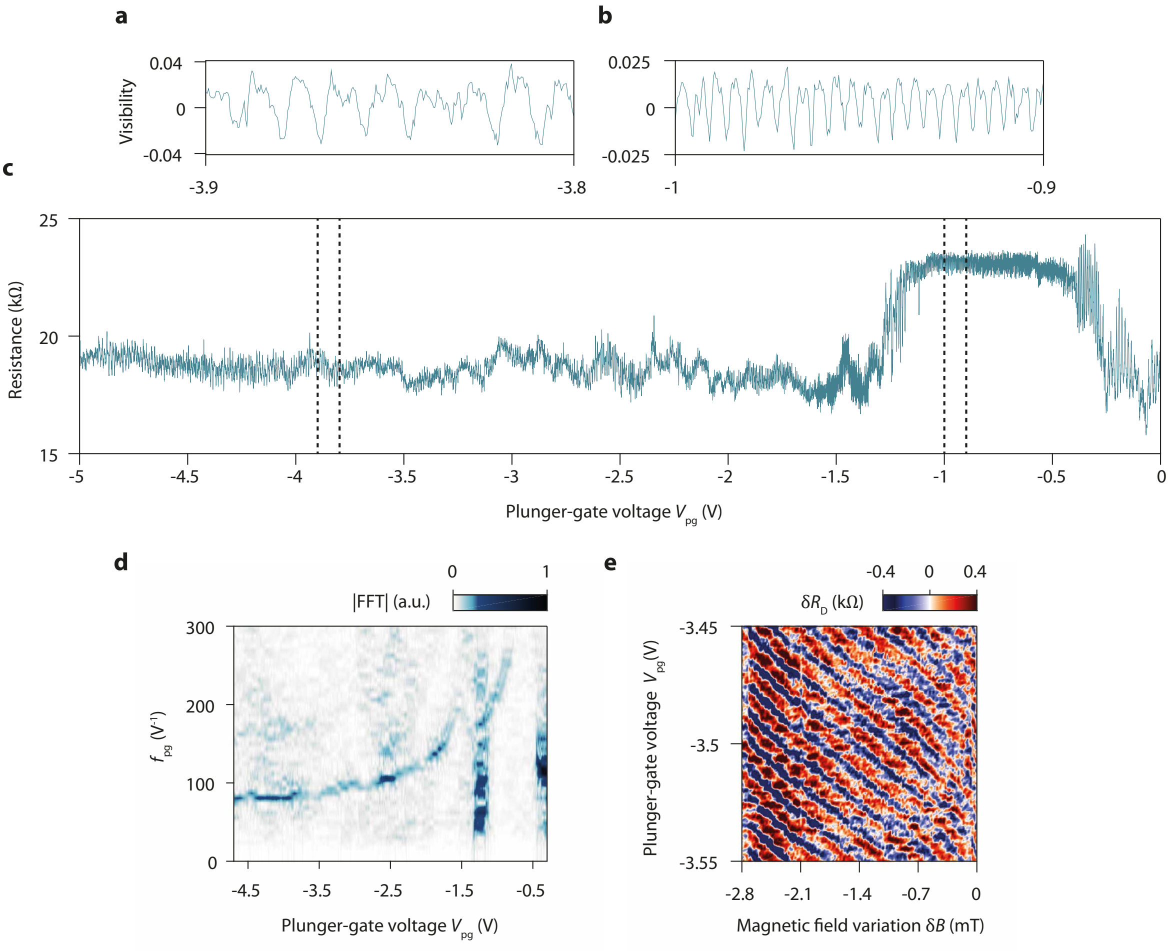

FIG. S14: **Resistance oscillations in sample BNGr30. a, b, c,** Resistance oscillations induced by a change of the plunger-gate voltage $V_{\rm pg}$ in interferometry experiments with the inner edge state at 14 T. The abrupt change in c of the mean resistance value at $V_{\rm pg} \approx -1.2$ V and $V_{\rm pg} \approx -0.2$ V might originate from instability of the QPCs. a and b show zooms on smaller $V_{\rm pg}$ ranges of the resistance oscillations converted in visibility $(R - \bar{R})/\bar{R}$, where $\bar{R}$ is the resistance background. **d,** Amplitude of the Fourier transform of resistance oscillations presented in c with respect to the plunger-gate voltage $V_{\rm pg}$ and the corresponding voltage frequency $f_{\rm pg}$. A continuous decrease of the oscillations frequency is observed while decreasing $V_{\rm pg}$. The divergence at $V_{\rm pg} \approx -1.2$ V is an artefact arising from the rapid change of the mean resistance value at this plunger-gate voltage. **e,** Evolution of the resistance oscillations with both the plunger-gate voltage $V_{\rm pg}$ and the magnetic field variation δB after subtraction of a resistance background for each plunger-gate voltage sweep. Constant $\delta R_{\rm D}$ lines have a negative slope characteristic of oscillations induced by the Aharonov-Bohm effect.

XIII. ABSENCE OF CHARGING EFFECT

Here we discuss the absence of Coulomb blockade in graphene FP interferometers. We follow the approach proposed in ref.[5,6] and estimate the relevant capacitances describing the electrostatics of the system. We use the notations of ref.[6], make approximate calculations for the small interferometer with a graphite back gate and discuss the case of the devices without graphite back gate. These calculations allow us to evaluate the parameter $\xi = \frac{C_{\rm eb}}{C_{\rm b}+C_{\rm eb}}$, where $C_{\rm b}$ is the bulk-to-gate capacitance and $C_{\rm eb}$ the edge-to-bulk capacitance, which defines according to Ref.[5] if the device is operating in the Aharonov-Bohm or Coulomb-dominated regime.

Bulk capacitance $C_{\rm b}$

The bulk capacitance $C_{\rm b}$ refers to the capacitance of the electrons located in the central part of the cavity and spatially separated from the conducting edge channels. These bulk electrons belong to the last partially-occupied Landau level and form an isolated island capacitively coupled to the gate electrodes[7] (back gate, plunger gates, and split-gates) . The electrostatic coupling of the bulk to the interfering edge channel is considered separately in another capacitance term $C_{\rm eb}$ discussed later.

For our device with a graphite back gate, the bulk capacitance is mostly given by $C_{\rm b} = C_{\rm bg}A_{\rm geo}$ where $C_{\rm bg} = 1.45$ mF/m^2 is the effective back-gate capacitance and $A_{\rm geo}$ is the geometrical area. For our small FP cavity, we obtain $C_{\rm b} = 4.5\times10^{-15}$ F. The corresponding bulk charging energy is thus $E_{\rm C} = \frac{e^2}{2C_{\rm b}} = 18\ \mu$eV comparable to that reported for devices in GaAs heterostructures[8] in which AB oscillations with fractional edge channels were reported.

For our devices without graphite back gate, the 285 nm thick SiO_2 layer gives $C_{\rm bg} = 0.12$ mF/m^2. Thus for devices having similar sizes, $C_{\rm b}$ is approximately decreased by a factor 10 with respect to devices with graphite back gate. For the two devices presented in section XII, BNGr64 and BNGr30, which respectively have geometrical surfaces of 11.5 and 10.1 μm^2, we obtain respectively $C_{\rm b} = 1.4$ and 1.2×10^{-15} F.

On top of this bulk-to-back-gate capacitance, one needs to add the contribution of the plunger-gate and split-gate electrodes resting atop the 20 nm thick capping hBN. This contribution is difficult to evaluate because the top gates are not located directly above the bulk island. However, they still provide an additional parallel capacitive coupling leading to an increase of $C_{\rm bg}$ and a reduction of the overall bulk charging energy. We note that this effect may play a significant role in devices on silicon substrate and may become the main contribution to the bulk capacitance.

Interfering edge channel capacitance $C_{\rm e}$

Similarly, the interfering edge channel is capacitively coupled to gates electrodes and one can define a edge-to-gates capacitance $C_{\rm e}$. For a sake of completeness, we also evaluate it though it does not appear in the expression of ξ. $C_{\rm e}$ is the sum of two contributions : the edge-to-top-gates capacitance $C_{\rm e/tg}$ and the edge-to-back-gate capacitance $C_{\rm e/bg}$.

The latter can be evaluated following a similar approach as above. In this case, $C_{\rm e/bg} = 2LwC_{\rm bg}$ where $2L$ is the FP cavity perimeter and w is the width of the compressible stripe corresponding to the QH edge channel. Assuming $w = l_B$ the magnetic length ($\approx$ 7 nm at 14 T), we obtain $C_{\rm e/bg} = 8.6 \times 10^{-17}$ F. This contribution is likely to be increased by edge-channel reconstruction[9], which could occurs along the smooth potential of the pn-junctions.

On the other hand, $C_{\rm e/tg} = C_{\rm e/sg} + C_{\rm e/pg}$ is the sum of the capacitance $C_{\rm e/sg}$ between the split-gates and the interfering edge channel and the capacitance $C_{\rm e/pg}$ between the plunger gate and the interfering edge channel. The latter can be extracted from the plunger-gate voltage period $\Delta V_{\rm pg}$ of AB oscillations, as an oscillation corresponds to the addition/removal of one flux quantum inside the area enclosed by the edge channel and thus of an electron in the corresponding Landau level. Then, $C_{\rm e/pg} = \frac{e}{\Delta V_{\rm pg}} = 1.6 \times 10^{-17}$ F for a typical voltage period $\Delta V_{\rm pg} = 10$ mV. Note that $C_{\rm e/pg}$ scales as the perimeter $L_{\rm pg}$ of the plunger gate (geometrically 1.5 μm). From this evaluation, we can also estimate $C_{\rm e/sg}$ by making the reasonable assumption that the electrostatics is the same for the split-gates and for the plunger gate. Thus $C_{\rm e/sg} = \frac{L_{\rm sg}}{L_{\rm pg}} C_{\rm e/pg} = 4.7 \times 10^{-17}$ F with $L_{\rm sg} = 4.4$ μm is the total length of the split-gate electrodes defining the cavity. The total edge capacitance is thus about $C_{\rm e} = 1.5 \times 10^{-16}$ F.

In devices with silicon back gate, we expect $C_{\rm e}$ to be lower due to a smaller $C_{\rm bg}$, but still of the same order of magnitude.

Edge-to-bulk capacitive coupling $C_{\rm eb}$

The capacitive coupling between the edge and the bulk is the most difficult contribution to evaluate. We base our estimation on ref.[10], which proposes a model to describe the transport in a quantum dot in the QH regime composed of a conducting island enclosed and coupled to a conducting ring. Equation (19) in ref.[10] allows to evaluate $C_{\rm eb}$ based on the charge distribution induced by a potential difference between the interfering edge channel and the bulk compressible island separated by a distance a. For simplicity, we assume this distance to be of the order of l_B in graphene by analogy with GaAs heterostructures (see eq. (38) of ref.[9] giving the width of innermost incompressible stripe). The calculation of the capacitance also requires to set a characteristic length scale d over which the influence of the potential difference is screened by nearby gate electrodes. For our device with a graphite back-gate electrode, this length scale is imposed by the thickness of the bottom hBN such that $d \simeq 20$ nm. In these conditions, we can write:

$$C_{\mathrm{eb}} = \frac{2L\epsilon_{\mathrm{BN}}\epsilon_0}{2\pi^2} \ln\left(\frac{4d}{a}\right), \tag{S1}$$

which leads to $C_{\mathrm{eb}} = 2.8 \times 10^{-17}$ F.

We expect that C_{eb} remains of the same order of magnitude for devices with silicon back gate because the various top gates around the FP cavity are also 20 nm away from the graphene flake and, hence, set the cutoff length d. More specifically, for our devices BNGr64 and BNGr30, which respectively have perimeters $2L = 15.1$ and 13.3 μm, we obtain $C_{\mathrm{eb}} = 5.0 \times 10^{-17}$ and 4.4×10^{-17} F. Alternatively, if we take $d = 285$ nm, we get $C_{\mathrm{eb}} = 10.4 \times 10^{-17}$ and 9.1×10^{-17} F.

Discussion

From these calculations, we can estimate the parameter $\xi = \frac{C_{\mathrm{eb}}}{C_{\mathrm{b}}+C_{\mathrm{eb}}}$. We obtain $\xi = 0.006$ for our 3.1 μm^2 device with graphite back gate, confirming that oscillations should arise from pure Aharonov-Bohm effect[5,6]. Similarly, for our devices with silicon back gate, we obtain $\xi = 0.03 - 0.07 \ll 1$ also consistent with the observation of oscillations in the AB regime. This analysis is fully consistent with the absence of charging effect in our graphene devices.

XIV. AHARONOV-BOHM OSCILLATIONS VERSUS DC VOLTAGE BIAS: ASYMMETRY AND DECAY

In this section, we discuss the oscillations induced by the application of a dc voltage bias and explain the origin of the tilted checkerboard pattern. We also analyze the decay of the oscillations amplitude with the voltage bias related to an energy relaxation or dephasing process.

Theoretical model for asymmetric potential drop

Here, we derive the formula for the transmission of a QH-FP interferometer as a function of magnetic field and voltage bias using the same formalism as in ref.[1], but we take into account a possible asymmetric potential drop at the two QPCs.

The transmission of a non-interacting QH Fabry-Pérot interferometer reads:

$$t(\epsilon, \Phi) = \frac{t_1 t_2 e^{i\pi\frac{\Phi}{\Phi_0} + i\frac{L\epsilon}{\hbar v}}}{1 - r_1^{\prime} r_2 e^{2i\pi\frac{\Phi}{\Phi_0} + i\frac{2L\epsilon}{\hbar v}}}, \tag{S2}$$

where $2\pi\frac{\Phi}{\Phi_0}$ is the Aharonov-Bohm phase, $\frac{2L\epsilon}{\hbar v}$ the dynamical phase accumulated by electrons after one winding in the cavity of length $2L$, t_1 and t_2 the transmission amplitudes of QPC$_1$ and QPC$_2$ for right moving particles, r_1' the reflection amplitude for left-movers at QPC$_1$ and r_2 the reflection amplitude for right-movers at QPC$_2$.

The transmission probability is:

$$T(\epsilon, \Phi) = \frac{\mid t_1 \mid^2 \mid t_2 \mid^2}{1 + \mid r_1^{\prime} r_2 \mid^2 - 2 \mid r_1^{\prime} r_2 \mid \cos(2\pi\frac{\Phi}{\Phi_0} + \frac{2L\epsilon}{\hbar v} + \varphi)}, \tag{S3}$$

where φ is a constant phase factor which depends on the scattering phase of the QPCs. Given that $\mid r_{1,2} \mid^2 = \mid r_{1,2}' \mid^2 = R_{1,2}$ and $\mid t_{1,2} \mid^2 = T_{1,2}$, we can rewrite (S3) as

$$T(\epsilon, \Phi) = \frac{T_1 T_2}{1 + R_1 R_2 - 2\sqrt{R_1 R_2}\cos(2\pi\frac{\Phi}{\Phi_0} + \frac{2L\epsilon}{\hbar v} + \varphi)}. \tag{S4}$$

In the weak backscattering limit, $R_i \ll 1$, and omitting the constant phase term φ, we obtain at first order:

$$T(\epsilon, \Phi) = 1 - R_1 - R_2 + 2\sqrt{R_1 R_2}\cos\left(2\pi\frac{\Phi}{\Phi_0} + \frac{2L\epsilon}{\hbar v}\right) \tag{S5}$$

We then consider a finite dc voltage bias V applied between source and drain contacts. We note $q = -e < 0$ the electron charge. Depending on the energy relaxation processes consecutive to the current flow, and on the electrostatic coupling between the cavity, the back gate, the source and the drain, the electrochemical potential in the cavity will adjust itself at a value intermediate between that of the source and that of the drain. The right-movers coming from the source contact have an energy $qV^+ = qV(\frac{1}{2}+x) = qV\beta$ with respect to the chemical potential within FP cavity and the left-movers coming from the drain have an energy $qV^- = -qV(\frac{1}{2}-x) = -qV\overline{\beta}$. In these expressions, $x \in [-\frac{1}{2}, \frac{1}{2}]$ is the voltage bias asymmetry factor. $x = 0$ corresponds to a symmetric biasing with $V^+ = \frac{V}{2}$ and $V^- = -\frac{V}{2}$, meaning that the potential drop is the same across both QPCs. When $x = \frac{1}{2}$ (or equivalently $x = -\frac{1}{2}$) the bias is completely asymmetric, $V^+ = V$ and $V^- = 0$ (or equivalently $V^+ = 0$ and $V^- = -V$), the potential drop only occurs at one QPC while the FP cavity is at the same potential as one of the two contacts.

At zero temperature, the current through the device is given by $I = \frac{q}{h}\int_{qV^-}^{qV^+} T(\epsilon,\Phi)\mathrm{d}\epsilon$. In the weak backscattering limit, it writes:

$$I = \frac{q}{h}\int_{qV^-}^{qV^+}\left[1 - R_1 - R_2 + 2\sqrt{R_1R_2}\cos\left(2\pi\frac{\Phi}{\Phi_0} + \frac{2L\epsilon}{\hbar v}\right)\right]d\epsilon = I_0 + I_{\rm osc}, \tag{S6}$$

where $I_0 = \frac{e^2}{h}(1-R_1-R_2)V$ is the constant part of the current and $I_{\rm osc}$ is the oscillating part of the current which writes:

$$I_{\rm osc} = \frac{e^2}{h}2\sqrt{R_1R_2}\frac{\hbar v}{2Lq}\left[\sin\left(2\pi\frac{\Phi}{\Phi_0} + \frac{2L}{\hbar v}qV\beta\right) - \sin\left(2\pi\frac{\Phi}{\Phi_0} - \frac{2L}{\hbar v}qV\overline{\beta}\right)\right]. \tag{S7}$$

The corresponding differential conductance is then:

$$\frac{dI_{\rm osc}}{dV} = g_{\rm osc}\left[\beta\cos\left(2\pi\frac{\Phi}{\Phi_0} - \frac{2L}{\hbar v}eV\beta\right) + \overline{\beta}\cos\left(2\pi\frac{\Phi}{\Phi_0} + \frac{2L}{\hbar v}eV\overline{\beta}\right)\right], \tag{S8}$$

with $g_{\rm osc} = \frac{e^2}{h}2\sqrt{R_1R_2}$ and restoring $q = -e$.

When the potential drop at the constrictions is symmetrical, that is, $V^+ = V/2$ and $V^- = -V/2$, we have $\beta = \overline{\beta} = \frac{1}{2}$ ($x = 0$) and then:

$$\frac{dI_{\rm osc}}{dV} = g_{\rm osc}\cos\left(2\pi\frac{\Phi}{\Phi_0}\right)\cos\left(2\pi\frac{L}{hv}eV\right), \tag{S9}$$

leading to a checkerboard pattern with a period versus bias voltage which is equal to the ballistic Thouless energy : $e\Delta V = hv/L = E_{\rm Th}$.

If the bias is completely asymmetrical, for example when $V^+ = V$ and $V^- = 0$ with $\beta = 1$ and $\overline{\beta} = 0$ ($x = \frac{1}{2}$), we obtain:

$$\frac{dI_{\rm osc}}{dV} = g_{\rm osc}\cos\left(2\pi\frac{\Phi}{\Phi_0} - 2\pi\frac{2L}{hv}eV\right) \tag{S10}$$

that draws a diagonal strip pattern with a period versus bias voltage (at fixed magnetic field) which is equal to half the Thouless energy. Any intermediate value of x leads to a mixed pattern, that is, a tilted checkerboard as observed in our experiment. Note that the measured diagonal resistance $\delta R_\mathrm{D} = -\frac{\mathrm{d}I_\mathrm{osc}}{\mathrm{d}V}(\frac{h}{e^2})^2$ shows exactly the same oscillatory features as the conductance in the weak backscattering limit.

In Fig. S15, we gather the results obtained in the three different interferometers as a function of voltage bias (Fig. S15a, c, d and f are respectively identical to Fig. 3c, d, e and f). The checkerboard patterns are tilted for our small (a) and medium interferometers (b), whereas the tilt is hardly visible for the largest interferometer (c). Using eq. (S8), we can quantitatively reproduce in Fig. S15d, e and f the three experimental checkerboards with asymmetry parameters $x = 0.2$, 0.1 and 0.02, respectively.

In our experiment, we apply a dc voltage to the source contact while the drain contact is kept grounded. The electrostatic coupling of the cavity to the back-gate electrode results in an asymmetric potential drop which could explain why the checkerboard patterns of our two smallest interferometers are tilted. On the other hand, the fact that the checkerboard pattern is nearly symmetric for the largest interferometer, indicates that energy relaxation processes equilibrate the chemical potential for sufficiently large interferometers, leading to a symmetric potential drop. Interestingly, tilted checkerboards in QH-FP interferometers has never been reported for GaAs QH-FP devices of the same size as our small interferometer, possibly due to the larger back-gate coupling in our graphene device equipped with a graphite back gate, or because the chemical potential equilibration is less effective in graphene.

Decay of the oscillations at finite bias

For an asymmetric potential drop characterized by an asymmetry factor x, the amplitude of the flux-periodic oscillations given by eq. (S8) oscillates versus bias voltage with the following dependence:

$$\mathcal{A}\left(V, E_\mathrm{Th}/e\right) = \sqrt{\cos^2\left(2\pi\frac{eV}{E_\mathrm{Th}}\right) + 4x^2\sin^2\left(2\pi\frac{eV}{E_\mathrm{Th}}\right)} \tag{S11}$$

Note that the period of this function is always the Thouless energy $E_\mathrm{Th} = hv/L$ whatever the asymmetry factor x, whereas the period of the conductance oscillations versus bias voltage at fixed magnetic field varies with the value of x (see for example eq. (S9) and eq. (S10)).

In Fig. S15a, b and c, however, we observe that the oscillations amplitude decays rapidly with the bias voltage and vanishes typically after one voltage period. Such a fast decay is much faster than the $1/\Delta V$ dependence predicted in ref.[1] and was already reported by McClure and coworkers[11] in GaAs QH-FP interferometers. These authors found that an exponential decay of the oscillations amplitude with the bias describes correctly the data. Theoretical investigations[12] confirmed that Coulomb interactions can lead to an approximate exponential decay. Following this approach, we fitted the oscillations in our data with:

$$\mathcal{A}(V, \Delta V_\mathrm{expo})\ \exp\left(-2\pi\chi\frac{|V|}{\Delta V_\mathrm{expo}}\right), \tag{S12}$$

where χ is a phenomenological parameter that describes how fast the oscillations vanish with voltage, and ΔV_{expo} is the period of the resistance oscillations for this exponential decay. The amplitude of the oscillations is obtained by computing the Fourier amplitude of the resistance oscillations as a function of the plunger-gate voltage at fixed bias voltage. This leads to the lobe structure shown in Extended Data Fig 4a, b and c. A good agreement between the model and the data is found for the three interferometers. The extracted voltage periods ΔV_{expo} and damping factors χ are reported in Table S3. It is worth noticing, however, that this phenomenological model does not capture the absence of secondary lobes in the experiments, suggesting that the decay of the oscillations is faster than exponential.

We therefore consider a second model with a Gaussian decay of the bias-induced oscillations. Investigations in Mach-Zehnder interferometers revealed that a Gaussian decay may arise from phase fluctuations of the interfering edge channel due to Coulomb interactions or the electric noise in the non-interfering edge channels[13–16]. Within this approach, we fitted our data with:

$$\mathcal{A}(V, \Delta V_{\mathrm{gauss}}) \exp\left(-\frac{V^2}{2{V_0}^2}\right), \tag{S13}$$

where V_0 is the voltage scale characterizing the width of the Gaussian envelope, and $\Delta V_{\mathrm{gauss}}$ the period of the resistance oscillation for this Gaussian decay. The fits of the experimental data with this expression are displayed in Extended Data Fig. 4a, b and c (orange lines). This second model also describes well the data. The extracted voltage periods $\Delta V_{\mathrm{gauss}}$, reported in Table S3, are close to those obtained with the exponential decay model. The extracted V_0 values scale linearly with the inverse interfering path length $1/L$ as mentioned in ref.[16] and is typically one third of $\Delta V_{\mathrm{gauss}}$.

The qualitative difference between the exponential and Gaussian decays is that the exponential decay fits better the amplitude of the first lobe but fails to reproduce the vanishing of the second ones, whereas the Gaussian model is less accurate for the first lobe but shows a suppressed second lobe.

QH-FP	ΔV_{expo} (μV)	χ	$\Delta V_{\mathrm{gauss}}$ (μV)	V_0 (μV)
Small	134	0.42	128	40
Medium	83	0.42	81	25
Large	57	0.35	61	21

TABLE S3: **Fitting parameters for the different models of bias-induced oscillation decay.** Voltage period ΔV_{expo} for the exponential decay model; χ damping rate for the exponential decay model; voltage period $\Delta V_{\mathrm{gauss}}$ for the Gaussian decay model; V_0 width of the Gaussian envelope.

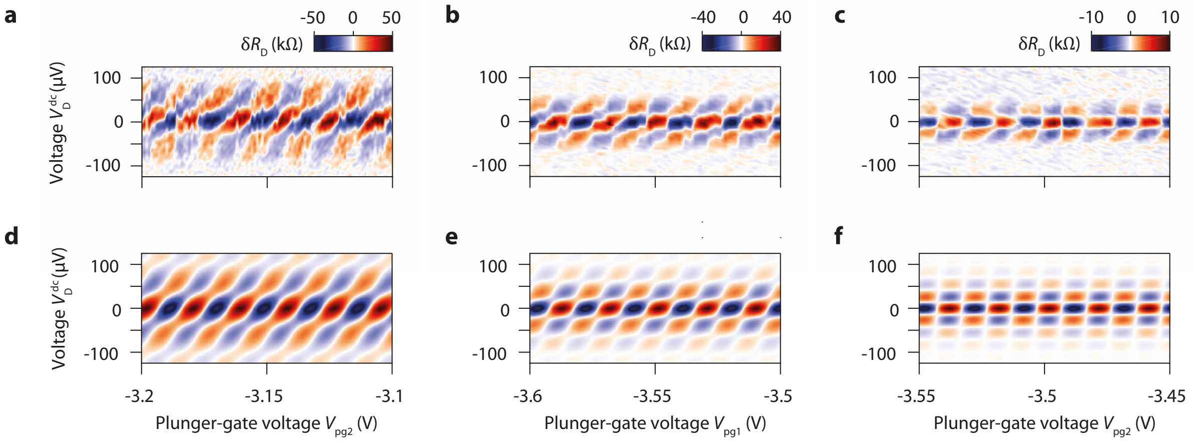

FIG. S15: **Bias dependence of Aharonov-Bohm oscillations. a, b, c,** Differential diagonal resistance variations δR_D, after background subtraction, versus dc diagonal voltage $V_{\mathrm{D}}^{\mathrm{dc}}$ and plunger-gate voltage $V_{\mathrm{pg1,2}}$ for the small, medium and large interferometer respectively in a, b and c. Interferences are obtained with the outer edge channel at 14 T. **d, e, f,** Numerical simulations of resistance oscillations induced by voltage bias and plunger-gate voltage that reproduce the data presented in a, b and c, respectively. The simulations incorporate an asymmetric potential drop at the two QPCs and an out-of-equilibrium decoherence factor. The voltage bias asymmetry factors of $x = 0.2$ and $x = 0.1$, respectively for the small d and medium interferometer e, are significant, indicating a limited chemical potential equilibration as opposed to the large interferometer f, which has a very small asymmetry term $x = 0.02$.

XV. TEMPERATURE DEPENDENCE OF THE AHARONOV-BOHM OSCILLATIONS: THERMAL AVERAGING

The effect of temperature on the visibility of the Aharonov-Bohm oscillations has been calculated in ref.[1] in the limit of weak backscattering and at finite bias voltage for a symmetric potential drop at the two constrictions. This calculation considers only the thermal averaging of the interference and does not introduce decoherence by inelastic scattering or energy relaxation at finite bias.

Here we explain in details the calculation in the symmetric case and then extend the result to the case of an asymmetric potential drop as observed in our device. In the following, we use the expression of the transmission coefficient obtained in the previous section in the limit of weak backscattering:

$$T(E,\Phi) = 1 - R_1 - R_2 + \sqrt{R_1 R_2}\left(e^{i2\pi\Phi/\Phi_0} e^{iE2L/\hbar v} + e^{-i2\pi\Phi/\Phi_0} e^{-iE2L/\hbar v}\right) \qquad \text{(S14)}$$

Symmetric potential drop

Assuming a symmetric potential drop at the two constrictions as in ref.[1], the current at finite temperature T and finite voltage V is given by:

$$I(\Phi,V,T) = \frac{q}{h}\int_{-\infty}^{+\infty} T(E,\Phi)\left(\frac{1}{1+e^{(E-\frac{qV}{2})/k_\mathrm{B}T}} - \frac{1}{1+e^{(E+\frac{qV}{2})/k_\mathrm{B}T}}\right)\mathrm{d}E, \qquad \text{(S15)}$$

where $q<0$ is the electron charge. Using the expression of the transmission coefficient in the limit of weak back-scattering, the current writes:

$$I(\Phi,V,T) = \frac{q^2}{h}(1-R_1-R_2)V - \frac{q}{h}\sqrt{R_1R_2}\left(e^{i2\pi\Phi/\Phi_0}H(V,T) + e^{-i2\pi\Phi/\Phi_0}H(V,T)^*\right), \qquad \text{(S16)}$$

where we introduce the function:

$$H(V,T) = \int_{-\infty}^{+\infty} e^{iE2L/\hbar v}\left(\frac{1}{1+e^{(E-\frac{qV}{2})/k_\mathrm{B}T}} - \frac{1}{1+e^{(E+\frac{qV}{2})/k_\mathrm{B}T}}\right)\mathrm{d}E. \qquad \text{(S17)}$$

By changing the variable in the integral, it becomes:

$$H(V,T) = \left(e^{i\frac{qV}{2}2L/\hbar v} - e^{-i\frac{qV}{2}2L/\hbar v}\right)\int_{-\infty}^{+\infty} e^{iE2L/\hbar v}\,\frac{1}{1+e^{E/k_\mathrm{B}T}}\,\mathrm{d}E, \qquad \text{(S18)}$$

where the choice of a symmetric potential drop influences only the term in the parenthesis. The calculation of the integral gives:

$$\int_{-\infty}^{+\infty} e^{iE2L/\hbar v}\,\frac{1}{1+e^{E/k_\mathrm{B}T}}\,\mathrm{d}E = -i2\pi k_\mathrm{B}T\sum_{n=0}^{+\infty} e^{-\omega_n 2L/\hbar v} = \frac{-i2\pi k_\mathrm{B}T}{2\sinh(\pi k_\mathrm{B}T2L/\hbar v)}, \qquad \text{(S19)}$$

where $\omega_n = (2n+1)\pi k_\mathrm{B} T$ are the Matsubara frequencies, with $n \in \mathbb{Z}$. In this case of a symmetric potential drop, the function $H(V,T)$ is real and writes:

$$H(V,T) = \sin(qVL/\hbar v)\,\frac{2\pi k_\mathrm{B} T}{\sinh(\pi k_\mathrm{B} T 2L/\hbar v)}. \tag{S20}$$

The current finally writes:

$$I(\Phi,V,T) = G_0 V - \frac{q}{h}\sqrt{R_1 R_2}\;\; 2\,\cos(2\pi\Phi/\Phi_0)\;\sin(qVL/\hbar v)\,\frac{2\pi k_\mathrm{B} T}{\sinh(\pi k_\mathrm{B} T 2L/\hbar v)}, \tag{S21}$$

which is equivalent to equations (16) and (18) in ref.[1]. The differential conductance writes:

$$G(\Phi,V,T) = G_0 - \frac{q^2}{h}\sqrt{R_1 R_2}\;\; 2\,\cos(2\pi\Phi/\Phi_0)\;\cos(qVL/\hbar v)\,\frac{\pi k_\mathrm{B} T 2L/\hbar v}{\sinh(\pi k_\mathrm{B} T 2L/\hbar v)}, \tag{S22}$$

which forms a checkerboard pattern as a function of field and voltage. At high temperature, the visibility of these oscillations decreases exponentially with a dependence of the form:

$$e^{-\pi k_\mathrm{B} T 2L/\hbar v} = e^{-4\pi^2 k_\mathrm{B} T/E_\mathrm{Th}} = e^{-T/T_0}, \tag{S23}$$

where $E_\mathrm{Th} = hv/L$ is the ballistic Thouless energy which corresponds to the oscillation period $q\Delta V$ versus bias voltage, and T_0 is the fitting parameter of the exponential temperature dependence which is related to the Thouless energy by:

$$4\pi^2 k_\mathrm{B} T_0 = E_\mathrm{Th} = q\Delta V. \tag{S24}$$

Asymmetric potential drop

In case of an asymmetric potential drop at the two constrictions (see section XIV), the potential energy is $qV^+ = \beta qV$ at the source contact and $qV^- = -\bar{\beta} qV$ at the drain contact, with $\beta = \frac{1}{2} + x$ and $\bar{\beta} = \frac{1}{2} - x$ with the parameter $x \in [-\frac{1}{2}, \frac{1}{2}]$ characterizing the asymmetry of the potential drop. The current at finite temperature T and finite voltage V is then given by:

$$I(\Phi,V,T) = \frac{q}{h}\int_{-\infty}^{+\infty} T(E,\Phi)\left(\frac{1}{1+e^{(E-\beta qV)/k_\mathrm{B} T}} - \frac{1}{1+e^{(E+\bar{\beta} qV)/k_\mathrm{B} T}}\right)\mathrm{d}E \tag{S25}$$

Following the same calculations as above now gives the function:

$$H(V,T) = e^{ixqV2L/\hbar v}\sin(qVL/\hbar v)\,\frac{2\pi k_\mathrm{B} T}{\sinh(\pi k_\mathrm{B} T 2L/\hbar v)} \tag{S26}$$

which contains a complex phase factor. The current writes:

$$I(\Phi,V,T) = G_0 V - \frac{q}{h}\sqrt{R_1 R_2}\;\; 2\,\cos(2\pi\Phi/\Phi_0 + xqV2L/\hbar v)\;\sin(qVL/\hbar v)\,\frac{2\pi k_\mathrm{B} T}{\sinh(\pi k_\mathrm{B} T 2L/\hbar v)} \tag{S27}$$

which is modified only by the term $xqV2L/\hbar v$ in the cosine function. The differential conductance writes:

$$G(\Phi, V, T) = G_0 - \frac{q^2}{h} \sqrt{R_1 R_2}\ \ 2\, g(\Phi, V)\, \frac{\pi k_{\mathrm{B}} T 2L/\hbar v}{\sinh(\pi k_{\mathrm{B}} T 2L/\hbar v)} \tag{S28}$$

where the oscillation term:

$$g(\Phi, V) = \cos(2\pi\Phi/\Phi_0 + xqV2L/\hbar v)\cos(qVL/\hbar v) - 2x\sin(2\pi\Phi/\Phi_0 + xqV2L/\hbar v)\sin(qVL/\hbar v) \tag{S29}$$

gives a titled checkerboard pattern as a function of field and voltage for $x \neq 0$. It is interesting to note that the temperature dependence is not affected by the asymmetry of the potential drop at the constrictions. The fitting parameter T_0 of the exponential temperature dependence is still related to the ballistic Thouless energy by $4\pi^2 k_{\mathrm{B}} T_0 = E_{\mathrm{Th}}$.

XVI. EVALUATION OF THE PHASE COHERENCE LENGTH L_ϕ

To estimate the phase coherence length L_ϕ in our graphene QH-FP interferometers, we assume that the visibility $\mathcal{V}$ of coherent oscillations scales as:

$$\mathcal{V} = \mathcal{V}_0 \frac{2L/L_T}{\sinh(2L/L_T)} \exp\left(-\frac{2L}{L_\phi(T)}\right) \tag{S30}$$

where $L_T = \frac{hv}{2\pi^2 k_B T}$ is the characteristic length associated with the decay of the visibility due to thermal averaging at temperature T (see eq. (S22) in previous section), $L_\phi(T)$ is the phase coherence length associated with extrinsic effects (that can depend on temperature), $2L$ is the the perimeter of the FP cavity and $\mathcal{V}_0$ is the asymptotic limit reached by the visibility when L tends to zero. In this expression, both thermal broadening (that acts as an internal phase decoherence between the different spectral components of the thermal electron wave packet) and extrinsic dephasing mechanisms add up and result in an effective decoherence length given by $1/L_\phi^*(T) = 1/L_T + 1/L_\phi$ for the limit of long interfering path lengths. Note that the exponential decrease due to the finite coherence length is only valid for $2L$ above L_ϕ and should saturate to a particular visibility below unity for smaller perimeters.

Fitting the evolution of $\mathcal{V}$ with $2L$ at fixed temperature with eq. (S30) provides a direct estimate of L_ϕ. As visibility depends on the QPC transmissions, we performed this length-dependence analysis by considering our best visibility data obtained for the three sizes of interferometers. We evaluate the electron temperature at our base fridge temperature to be $T \simeq 20$ mK, which corresponds to the temperature below which the T-dependence of the visibility saturates. For experiments with the inner edge channel, we extracted the visibility through $\frac{G_{\max}-G_{\min}}{(G_{\max}-e^2/h)+(G_{\min}-e^2/h)}$, which subtracts the conductance contribution of the fully transmitted outer edge channel.

Extended Data Figure 5 shows the evolution of these visibilities $\mathcal{V}$ with the perimeter of the interferometers $2L$. For comparison, the decrease of the visibility induced by the thermal broadening at 20 mK is also shown with the solid red line (eq. (S30) with $L_\phi(T)$ infinite and a edge state velocity of 1.4×10^5 m/s, giving $L_T = 17$ μm). For both experiments with the outer and the inner edge channel, a fast decrease of $\mathcal{V}$ with $2L$ is observed which cannot be explained by the effect of thermal broadening. The best visibilities for both interfering edge channels are virtually the same except for data in the large interferometer with the inner edge channel, which shows a significant drop compared to the data with the outer one. It probably reflects that the tuning of the QPC could have been improved. We thus discard it for our quantitative analysis.

By fitting the visibility decay, we extract a phase coherence length $L_\phi \approx 10$ μm at 20 mK. We estimate the electron temperature as the temperature below which the visibility does not increase anymore, which is about 20 mK. The obtained value of 10 μm is smaller or comparable to the perimeter length, which justifies the exponential decrease used in eq. (S30) (the saturation would appear for smaller perimeters as the ones studied here). This value is also consistent with the observation of coherent Aharonov-Bohm oscillations in the double FP cavity at base temperature.

XVII. ANALYSIS OF THE DOUBLE-CAVITY INTERFEROMETER

In this section we discuss the experiments performed in the coherently-coupled double FP cavity. We first derive the theoretical expression for the transmission for a double cavity and then compare it with our data to show that electron transport remains coherent in the overall device.

The transmission and reflection amplitudes of a Fabry-Pérot interferometer reads:

$$t_{\text{FP}}(\varphi) = \frac{t_1 t_2 e^{i\varphi}}{1 - r_1' r_2 e^{i2\varphi}}, \tag{S31}$$

$$t'_{\text{FP}}(\varphi) = \frac{t_1' t_2' e^{i\varphi}}{1 - r_1' r_2 e^{i2\varphi}}, \tag{S32}$$

$$r_{\text{FP}}(\varphi) = r_1 + \frac{r_2 t_1 t_1' e^{i2\varphi}}{1 - r_1' r_2 e^{i2\varphi}}, \tag{S33}$$

$$r'_{\text{FP}}(\varphi) = r_2' + \frac{r_1' t_2' t_2 e^{i2\varphi}}{1 - r_1' r_2 e^{i2\varphi}}, \tag{S34}$$

where 2φ is the Aharonov-Bohm phase accumulated by electrons after one winding in the cavity, t_i (t_i') the transmission amplitude, and r_i (r_i') the reflection amplitude of QPC$_i$ for right (left) moving particles.

The total transmission amplitude t_{tot} of two coupled FP cavities can be calculated using the transmission and reflection amplitudes of one FP cavity and the transmission and reflection amplitudes of a third QPC. Thus, using the previous expressions, we have:

$$t_{\text{tot}}(\varphi_1, \varphi_2) = \frac{t_{\text{FP}}(\varphi_1) t_3 e^{i\varphi_2}}{1 - r'_{\text{FP}}(\varphi_1) r_3 e^{i2\varphi_2}}, \tag{S35}$$

where $2\varphi_1$ and $2\varphi_2$ are the Aharonov-Bohm phase accumulated by electrons after one winding in the cavity between QPC$_1$ and QPC$_2$ and between QPC$_2$ and QPC$_3$, respectively.

Using $|t_i|^2 = |t_i'|^2 = T_i$, $|r_i|^2 = |r_i'|^2 = R_i$ and the relation $r_i' = -\bar{r}_i t_i' / \bar{t}_i$ (the overline indicates complex conjugate), we can express the transmission as:

$$T_{\text{tot}}(\phi_1, \phi_2) = \frac{T_1 T_2 T_3}{|1 - \sqrt{R_1 R_2} e^{i\phi_1} - \sqrt{R_2 R_3} e^{i\phi_2} + \sqrt{R_1 R_3} e^{i(\phi_1 + \phi_2)}|^2} = \frac{T_1 T_2 T_3}{D}, \tag{S36}$$

where ϕ_1 and ϕ_2 are the Aharonov-Bohm phases acquired when quasiparticles wind into the medium and small cavities respectively (including the phase factor from the reflection amplitudes of the QPCs). The denominator D can be written as:

$$\begin{aligned} D = 1 + R_1 R_2 + R_3 R_2 + R_1 R_3 - 2(1 + R_3)\sqrt{R_1 R_2} \cos(\phi_1) - 2(1 + R_1)\sqrt{R_2 R_3} \cos(\phi_2) \\ + 2\sqrt{R_1 R_3} \cos(\phi_1 + \phi_2) + 2R_2 \sqrt{R_1 R_3} \cos(\phi_1 - \phi_2). \end{aligned} \tag{S37}$$

In this expression, four oscillation frequencies emerge, namely, ϕ_1, ϕ_2, $\phi_3 = \phi_1 + \phi_2$ and $\phi_4 = \phi_1 - \phi_2$. The terms in ϕ_3 and ϕ_4 in eq. (S37), which result from coherent interferences through the two interferometers, does not have the same prefactor : the amplitude of the ϕ_3 oscillations is larger than the amplitude of the ϕ_4 oscillations which is even negligible in the weak backscattering limit. In contrast, in a situation where the transport through the double cavity would be incoherent, one could expect the appearance of term in the form of $\cos(\phi_1) \times \cos(\phi_2) = \frac{1}{2}\left[\cos(\phi_3) + \cos(\phi_4)\right]$ which would lead to equal amplitudes of ϕ_3 and ϕ_4 oscillating components.

Relating this model to our device geometry, we can ascribe to each of these four Aharonov-Bohm fluxes a coupling to the relevant plunger gates:

$$\phi_1 \simeq \frac{2\pi}{\Phi_0}(\delta A_1 B + A_1 \delta B) = \frac{2\pi}{\Phi_0}(\alpha_1 V_{\mathrm{pg1}} B + A_1 \delta B), \tag{S38}$$

$$\phi_2 \simeq \frac{2\pi}{\Phi_0}(\delta A_2 B + A_2 \delta B) = \frac{2\pi}{\Phi_0}(\alpha_2 V_{\mathrm{pg2}} B + A_2 \delta B), \tag{S39}$$

$$\phi_3 \simeq \frac{2\pi}{\Phi_0}\left[(\delta A_1 + \delta A_2)B + (A_1 + A_1)\delta B\right] = \frac{2\pi}{\Phi_0}\left[(\alpha_1 V_{\mathrm{pg1}} + \alpha_2 V_{\mathrm{pg2}})B + (A_1 + A_2)\delta B\right], \tag{S40}$$

$$\phi_4 \simeq \frac{2\pi}{\Phi_0}\left[(\delta A_1 - \delta A_2)B + (A_1 - A_2)\delta B\right] = \frac{2\pi}{\Phi_0}\left[(\alpha_1 V_{\mathrm{pg1}} - \alpha_2 V_{\mathrm{pg2}})B + (A_1 - A_2)\delta B\right], \tag{S41}$$

where A_1 and A_2 are the area of the medium and small cavities, respectively, V_{pg1} and V_{pg2} the plunger-gate voltages that tune these areas and α_1 and α_2 their lever arms.

In Figure S16 we show the expected frequencies in Fourier space for a coherently-coupled double QH-FP interferometer upon varying both plunger gates (Fig. S16a), or one plunger gate and the magnetic field (Fig. S16b and c). For the former case, the plunger-gate frequencies corresponding to the small and medium interferometers are located on the x and y axis, reflecting the terms ϕ_1 and ϕ_2 in eq. (S37), whereas the double interferometer terms ϕ_3 and ϕ_4 that depend on both plunger gates are located on the diagonals. For latter configurations, the frequency of the interferometer without the active plunger gate depends only on B and is thus located at zero plunger-gate frequency on the horizontal axis (ϕ_1 in b and ϕ_2 in c), whereas the frequency of the other interferometer with the active plunger gate, as well as the coupled interferometer frequencies, are located at finite plunger gate frequency.

In Figure S17 we reproduce the data shown in Fig. 4 for the coherently-coupled QH-FP interferometer and add the configuration with V_{pg1} active and magnetic field (Fig. S17c), which provides another confirmation of the presence of the ϕ_3 contribution. The four quadrants of the Fourier amplitudes are shown in order to check the presence of the $\phi_4 = \phi_1 - \phi_2$ frequency. The ϕ_4 frequency, whose expected location is

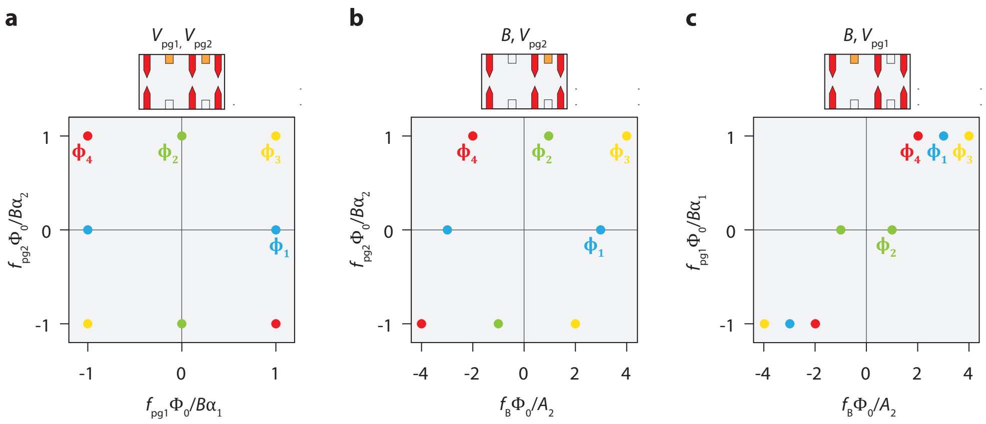

FIG. S16: **Fourier analysis of double QH-FP interferometer. a, b, c,** Positions in reciprocal space of the oscillation frequencies for three different configurations of interferometry experiments (assuming $A_1 = 3A_2$). Each peak is labelled with its Aharonov-Bohm phase. Top schematics depict the active QPCs (red) and plunger gates (orange) in each experiments. The parameters used to tune the Aharonov-Bohm phases in each case are indicated above the corresponding schematic.

indicated by the red circle in Fig. S17d-f, is clearly present in the configuration of Fig. S17e. Its amplitude is smaller than the amplitude of the ϕ_3 contribution as expected in eq. (S37). For the two other configurations, this ϕ_4 frequency is hardly visible. This detailed analysis provides compelling evidence for coherent transport through the three QPCs.

We can furthermore simulate the data by a simplified model that neglects terms in R^2 in eq. (S37):

$$\delta R = \delta R_1 \cos(\phi_1) + \delta R_2 \cos(\phi_2) + \delta R_3 \cos(\phi_3). \quad \text{(S42)}$$

Using the experimental Fourier amplitudes for the parameters δR_1, δR_2 and δR_3 we obtain the resistance maps shown in Fig. S17g-i that reproduce the experimental maps in Fig. S17a-c with excellent fidelity.

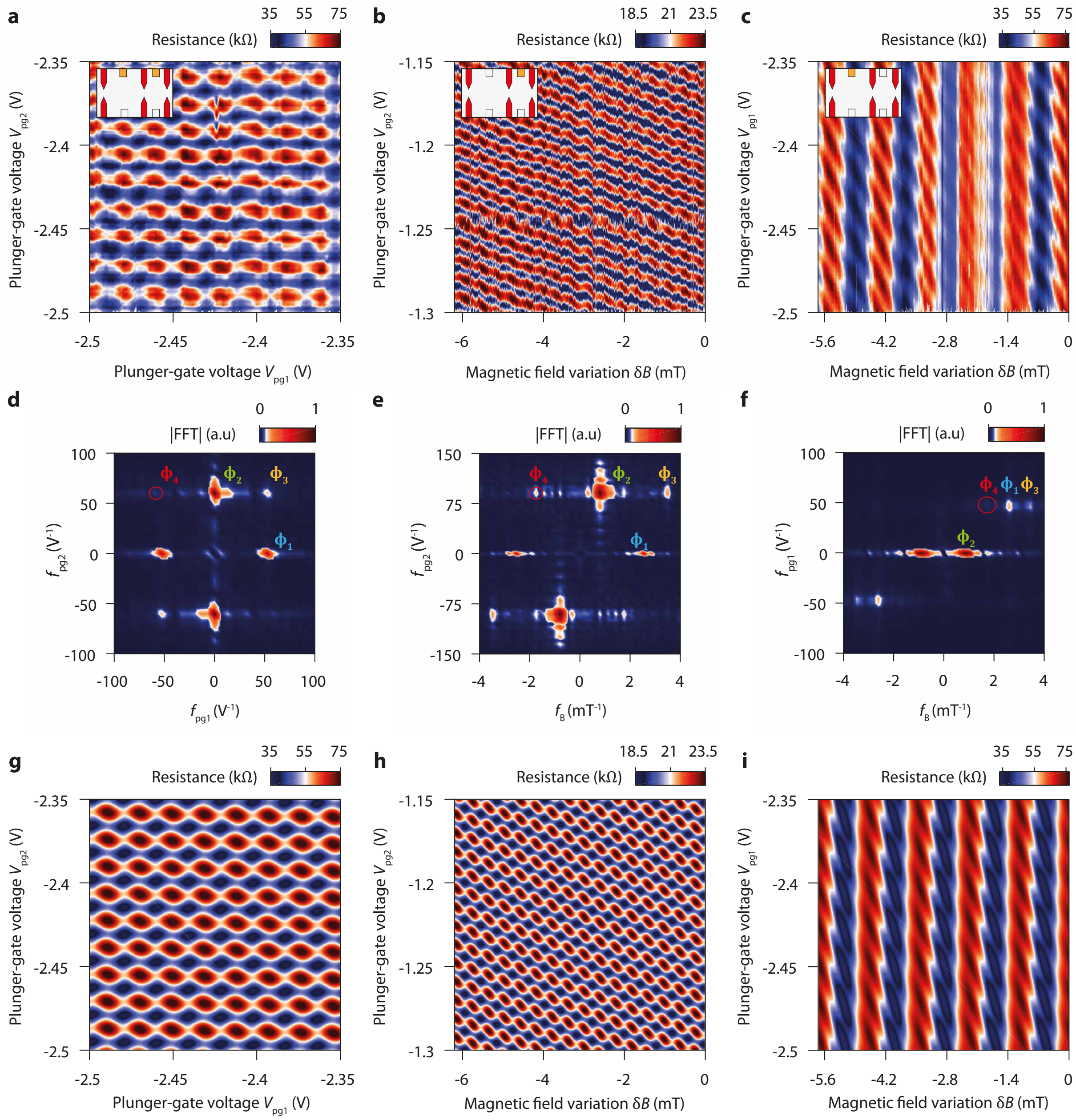

FIG. S17: **Coherently-coupled double QH-FP interferometer. a,** Diagonal resistance versus plunger-gate voltages V_{pg1} and V_{pg2} (outer edge channel interfering, B = 14 T). **b,** Diagonal resistance versus magnetic field variation δB and plunger-gate voltage V_{pg2} (inner edge channel interfering, B = 14 T). **c,** Diagonal resistance versus magnetic field variation δB and plunger-gate voltage V_{pg1} (outer edge channel interfering, B = 14 T). The inset schematics in a, b and c indicate the active QPCs (in red) and plunger gates (in orange) for the respective measurements. a and b are identical to the Fig. 4c and 4d of the main text. **d, e, f,** Four-quadrant Fourier amplitude of the resistance oscillations displayed respectively in a, b and c in their respective reciprocal space. The peaks corresponding to the different Aharonov-Bohm phases are identified in each case. **g, h, i,** Numerical simulations reproducing the experiments shown respectively in a, b and c with eq. (S42). The parameters (δR_1, δR_2, δR_3) are (0.66, 1, 0.18) in g, (0.64, 1, 0.22) in h, and (0.19, 1, 0.11) in i.

[1] Chamon, C., Freed, D. E., Kivelson, S. A., Sondhi, S. L. & Wen, X. G. Two point-contact interferometer for quantum Hall systems. *Phys. Rev. B* **55**, 2331–2343 (1997).

[2] Zimmermann, K. *et al.* Tunable transmission of quantum Hall edge channels with full degeneracy lifting in split-gated graphene devices. *Nature Commun.* **8**, 14983 (2017).

[3] Veyrat, L. *et al.* Low-Magnetic-Field Regime of a Gate-Defined Constriction in High-Mobility Graphene. *Nano Letters* **19**, 635–642 (2019).

[4] Liu, M. Theory of carrier density in multigated doped graphene sheets with quantum corrections. *Phys. Rev. B* **87**, 125427 (2013).

[5] Halperin, B. I., Stern, A., Neder, I. & Rosenow, B. Theory of the Fabry-Pérot quantum Hall interferometer. *Phys. Rev. B* **83**, 155440 (2011).

[6] Sivan, I. *et al.* Observation of interaction-induced modulations of a quantum Hall liquid's area. *Nature Commun.* **7**, 12184 (2016).

[7] Rosenow, B. & Halperin, B. I. Influence of Interactions on Flux and Back-Gate Period of Quantum Hall Interferometers. *Phys. Rev. Lett.* **98**, 106801 (2007).

[8] Nakamura, J. *et al.* Aharonov-Bohm interference of fractional quantum Hall edge modes. *Nature Physics* **15**, 563–569 (2019).

[9] Chklovskii, D. B., Shklovskii, B. I. & Glazman, L. I. Electrostatics of edge channels. *Phys. Rev. B* **46**, 4026–4034 (1992).

[10] Evans, A. K., Glazman, L. I. & Shklovskii, B. I. Coulomb blockade in the quantum-Hall-effect state. *Phys. Rev. B* **48**, 11120 (1993).

[11] McClure, D. T. *et al.* Edge-state velocity and coherence in a quantum Hall Fabry-Pérot interferometer. *Phys. Rev. Lett.* **103**, 206806 (2009).

[12] Ngo Dinh, S. & Bagrets, D. A. Influence of Coulomb interaction on the Aharonov-Bohm effect in an electronic Fabry-Pérot interferometer. *Phys. Rev. B* **85**, 073403 (2012).

[13] Roulleau, P. *et al.* Finite bias visibility of the electronic Mach-Zehnder interferometer. *Phys. Rev. B* **76**, 161309 (2007).

[14] Roulleau, P. *et al.* Noise Dephasing in Edge States of the Integer Quantum Hall Regime. *Phys. Rev. Lett.* **101**, 186803 (2008).

[15] Litvin, L. V., Helzel, A., Tranitz, H., Wegscheider, W. & Strunk, C. Edge-channel interference controlled by Landau level filling. *Phys. Rev. B* **78**, 075303 (2008).

[16] Yamauchi, Y. *et al.* Universality of bias- and temperature-induced dephasing in ballistic electronic interferometers. *Phys. Rev. B* **79**, 161306 (2009).